Optics Letters

Single-resonance silicon nanobeam filter with an ultra-high thermo-optic tuning efficiency over a wide continuous tuning range

Yong Zhang,[1] Yu He,[1] Qingming Zhu,[1] Xuhan Guo,[1] Ciyuan Qiu,[1] Yikai Su,[1,*] and Richard Soref[2]

[1]State Key Lab of Advanced Optical Communication Systems and Networks, Department of Electronic Engineering, Shanghai Jiao Tong University, Shanghai 200240, China
[2]Engineering Department, University of Massachusetts, Boston, Massachusetts 02125, USA
*Corresponding author: yikaisu@sjtu.edu.cn

Received 25 June 2018; accepted 13 August 2018; posted 20 August 2018 (Doc. ID 336078); published 14 September 2018

Energy-efficient tunability is highly desired for silicon photonic devices. We demonstrate a thermo-optic tunable filter with an ultra-high tuning efficiency based on a suspended photonic crystal nanobeam cavity. Attributed to the ultra-small mode volume and free-standing waveguide structure, a tuning efficiency of 21 nm/mW is achieved over a wide single-resonance tuning range of ∼43.9 nm. The 10%–90% switching times are 67.0 μs and 68.8 μs for the rising edge and the falling edge, respectively. The demonstrated energy-efficient tunable device can find applications in reconfigurable photonic integrated circuits.

OCIS codes: (130.3120) Integrated optics devices; (130.7408) Wavelength filtering devices; (230.5750) Resonators.

https://doi.org/10.1364/OL.43.004518

Silicon photonics is a promising candidate to meet the requirements of low energy consumption, high speed, high density, and low cost in data centers, optical communications, and high-performance computing [1–5]. Highly energy-efficient tunability is desired for silicon photonic devices [6,7]. Compared to electro-optic tuning, thermo-optic tuning shows the advantages of large refractive index change and negligible optical loss [8–11]. Silicon has a high thermo-optic coefficient of 1.86×10^{-4}/K, with a resonance wavelength shift of ∼80 pm/K [12]. Generally, thermo-optic tuning is achieved by applying a metallic microheater on a silicon waveguide [13,14]. A SiO_2 layer is needed between the silicon waveguide and the metallic microheater to avoid the light absorption induced by the metal. The typical tuning efficiency of this structure is ∼0.25 nm/mW and limited by the high heat capacity [15,16], which is attributed to the low thermal conductivity of SiO_2 (1.44 $Wm^{-1} K^{-1}$) [17]. Several methods have been proposed to achieve high tuning efficiency, including integrating the microheater directly on the silicon [18], suspended waveguide structures [19], and different doping levels of the waveguides [20]. A tuning efficiency of 1.8 nm/mW was demonstrated in an adiabatic resonant microring [18]. Higher tuning efficiency of 4.8 nm/mW but slower tuning speed of 170 μs was achieved in a silicon racetrack resonator with air trenches and a substrate undercut structure [12]. However, these devices show multiple resonances in an operation band. Higher tuning efficiency with a single resonance over a wide band is highly desired for silicon tunable filters. Silicon photonic crystal (PhC) nanobeam cavities offer an approach to improve the light–matter interaction due to their ultra-small mode volumes [21,22]. It has been used in many applications, including ultra-low threshold lasers [23,24], on-chip light sources [25,26], sensors [27,28], and optical switches [29,30]. A tunable PhC nanobeam cavity was theoretically proposed and numerically studied to achieve low power consumption and a single resonance [31].

In this Letter, we experimentally demonstrate a suspended silicon PhC nanobeam filter with an ultra-high thermo-optic tuning efficiency over a wide tuning range. The high tuning efficiency is 21 nm/mW, which is four times that of the reported highest result [12]. The device shows a single resonance with a continuous tuning range of ∼43.9 nm. Although the required tuning power per free spectral range (FSR) is fixed for a resonator, in practical applications where the FSR is wider than the operation band, tuning efficiency (nm/mW or mW/nm) is more suitable to characterize the wavelength tunability [31]. The high efficiency and the wide tuning range are attributed to the ultra-small mode volume of the PhC nanobeam cavity and its suspended waveguide structure. By etching away the silica layer under the PhC nanobeam cavity and adding thermal insulation trenches, the PhC nanobeam cavity is suspended in air. The heat generated by a metallic microheater can be localized around the PhC nanobeam cavity due to the lower thermal conductivity of the air. In addition, the response of the device is ∼68 μs by integrating the microheater directly on the silicon slab to reduce the heat capacity, which is more than 2.5 times faster than results for the suspended-structure devices [12,32].

In a PhC nanobeam cavity, a periodic array of air holes is etched into a waveguide. The nanobeam cavity can be viewed as

a wavelength-scale Fabry–Perot cavity with PhC mirrors [21], as shown in Fig. 1(a). The device is designed on a silicon-on-insulator (SOI) platform (220-nm-thick silicon on 3-μm-thick SiO_2). The ridge width of the nanobeam waveguide is 610 nm, and the height of the silicon slab is 50 nm. The PhC mirror pitch $a = 430$ nm is linearly tapered over a five-hole section to $a = 330$ nm at the cavity center. The radius of the holes also varies and is equal to 0.42a. The number of the air holes N on each PhC mirror is six. Figure 1(a) shows the electric field distribution of the transverse electric (TE)-polarized PhC nanobeam cavity, simulated by the three-dimensional finite-difference time-domain (3D-FDTD) method. The calculated mode volume of the nanobeam cavity is ~0.344 μm^3. Figures 1(b)–1(d) show the 3D view, top view, and yz cross section of the suspended thermo-optic tunable nanobeam filter, respectively. By etching away the silica layer under the PhC nanobeam cavity by a dilute hydrofluoric (HF) acid solution and adding thermal insulation trenches, the PhC nanobeam cavity is suspended in air. The length and width of the thermal insulation trench are 28 μm and 5 μm, respectively. Benefiting from the low thermal conductivity of air, the heat can be localized around the nanobeam cavity, thus high tuning efficiency and low power consumption can be achieved. A metallic microheater is placed directly on the silicon slab to improve the tuning speed, due to the high thermal conductivity of silicon (80 $Wm^{-1} K^{-1}$) [33]. The microheater material is chosen to be platinum (Pt), which cannot be etched by a dilute HF acid solution. The thickness, width, and length of the Pt microheater are 300 nm, 1 μm, and 24 μm, respectively. The gap between the microheater and the PhC nanobeam cavity is 650 nm. A smaller gap can improve the tuning efficiency, at the cost of increased light absorption loss induced by the metal.

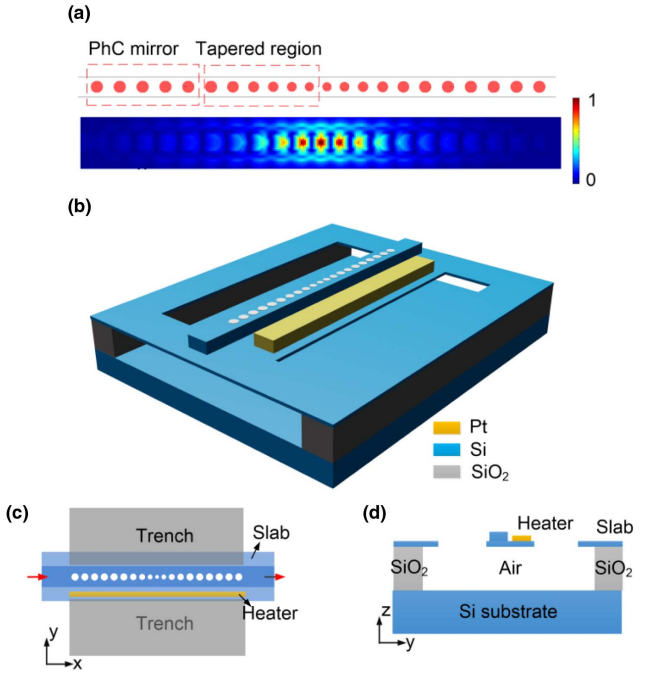

Fig. 1. (a) Structure and electric field distribution of a PhC nanobeam cavity. (b)–(d) 3D view, top view, and yz cross section of the suspended thermo-optic tunable nanobeam filter, respectively.

We use 3D finite element method (FEM) simulations to study the temperature distribution of the device in the heating process. Figures 2(a) and 2(b) depict the 3D temperature distribution in the PhC nanobeam filter and the thermal distribution in the xy cross section of the device when the heating power is 1 mW, respectively. The thermal field is localized around the area of the PhC nanobeam cavity. The temperature of the silicon in the suspended nanobeam cavity increases from 293 K to 665 K, indicating that the simulated tuning efficiency is 29.76 nm/mW.

The PhC nanobeam devices were fabricated on a SOI wafer (220-nm-thick silicon on 3-μm-thick SiO_2). Grating couplers, ridge silicon waveguides, PhC nanobeam cavities, and air trenches were patterned and etched by e-beam lithography

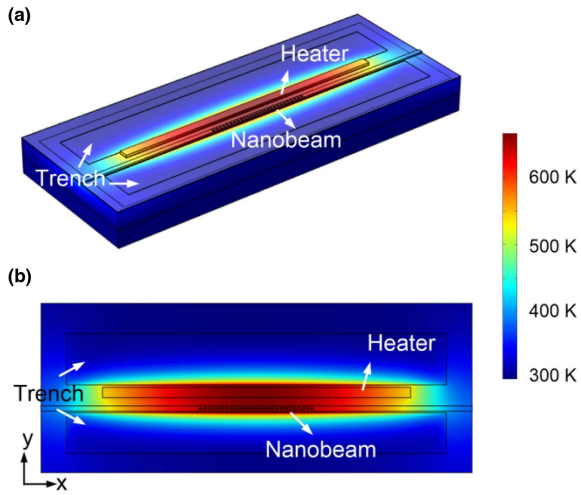

Fig. 2. (a) 3D temperature distribution of the suspended nanobeam device. (b) Thermal field distribution in the xy cross section of the suspended nanobeam device. Thermal field distributions are calculated by the 3D-FEM method.

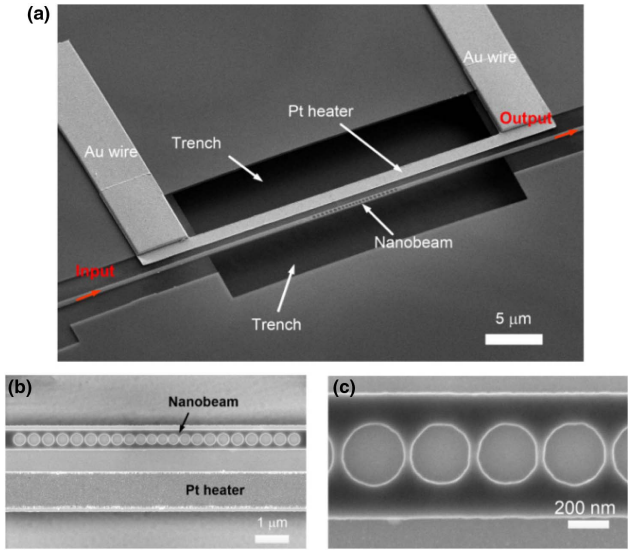

Fig. 3. (a) SEM photo of a fabricated PhC nanobeam filter. (b) and (c) Magnified SEM photos of the PhC nanobeam cavity.

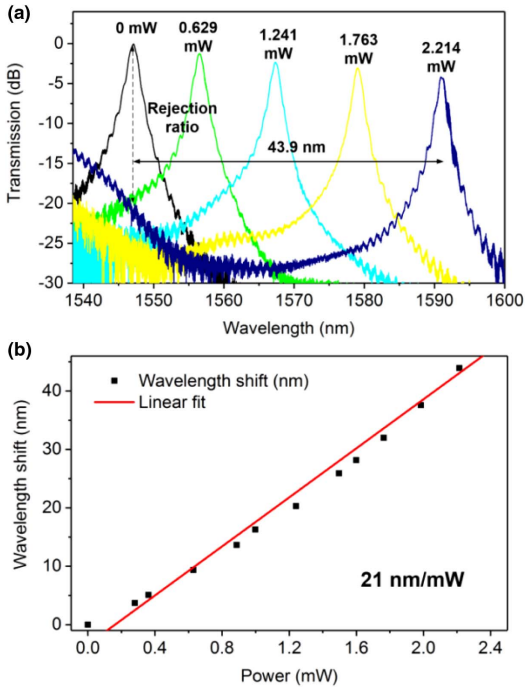

Fig. 4. (a) Measured transmission spectra with different heating powers. (b) Measured wavelength shifts as a function of heating powers.

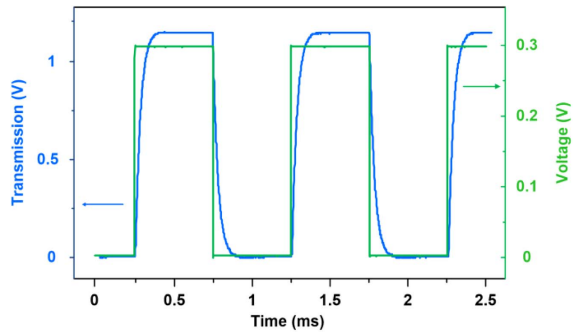

Fig. 5. Temporal response of the suspended nanobeam filter. The green and blue curves represent the square-wave drive signal and the optical transmission of the device, respectively.

(Vistec EBPG 5200+) and inductively coupled plasma (ICP) etching (SPTS DRIE-I). Then, Pt (300 nm) was sputtered on the silicon slab to form the 1-μm-wide microheaters. Gold (Au, 300 nm) was evaporated to define the electrical wires and contact pads using a lift-off process. Finally, the silica layer beneath the PhC nanobeam cavity was removed by a dilute HF acid solution to form the free-standing structure. The scanning electron microscope (SEM) photos of a fabricated suspended nanobeam filter are shown in Figs. 3(a)–3(c). The suspended membrane is supported by the silicon ridge waveguide to avoid bending. The footprint of the nanobeam cavity region with air holes is 8.5 μm × 2.2 μm. In the measurements, TE-polarized grating couplers were used to couple the light into/out of the silicon chip. The period of the TE-polarized grating coupler is 630 nm, and the filling factor is 48%. The etching depth is 70 nm. The coupling loss of the TE-polarized grating couplers is 5.35 dB/port at 1550 nm. The 3-dB bandwidth is 60 nm. A broadband amplified spontaneous emission (ASE) source, an optical spectrum analyzer (OSA) (Yokogawa AQ6370B), and a voltage-current source-meter (Keithley 2400) were used to characterize the thermo-optic tunable devices.

Figure 4(a) shows the transmission spectra of a fabricated PhC nanobeam filter with different heating powers. The responses are normalized to the transmission of a grating-coupled straight ridge waveguide. When no heating power is applied, the filtering wavelength is 1547.068 nm, the insertion loss is 0.05 dB, and the 3-dB bandwidth is 1.58 nm. When the applied heating power is increased to 2.214 mW, the filtering wavelength is shifted to 1591.004 nm, indicating a wide single-resonance tuning range of >43.9 nm. The inter-channel rejection ratio defines the undesired signal from another filtering channel. The inter-channel rejection ratio of >20 dB can be obtained over a 43.9-nm range, satisfying error-free operation with most modulation formats [34] for multi-wavelength channels. A higher rejection ratio can be achieved by cascading silicon nanobeam cavities and optimizing the pitch and the radius of the air holes. It is seen that the insertion loss increases during the thermal tuning process, which may be attributed to non-uniform heating over the cavity. Figure 4(b) shows the measured filtering wavelength shifts with different heater powers. In total, we measured 12 data sets, while in Fig. 4(a) we show only five evenly spaced ones to distinguish the traces. The measured data are fitted to obtain a thermal tuning efficiency of 21 nm/mW. Such a high efficiency and a wide tuning range are enabled by the ultra-small mode volume and the suspended waveguide structure of the PhC nanobeam cavity. The heating power for full-FSR tuning is estimated to be ~5 mW.

We also measured the tuning speed for the free-standing tunable filter by driving the heater with a 1-kHz square-wave

Table 1. Comparisons of Various Silicon Thermo-Optic Tunable Filters

	Tuning Efficiency (nm/mW)	Tuning Range (nm)	Rejection Ratio (dB)	Insertion Loss (dB)	Response Time (μs)	Single Resonance
Microring [16]	0.29	20	25	/	14	No
Microring with trenches [35]	0.9	7.75	~22	<5	9	No
Suspended racetrack [12]	4.8	11.5	~10	<2	170	No
Adiabatic resonant microrings [18]	1.84	32.85	~15	~7	1	No
Nanobeam [27]	0.015	6.8	21	<2	13	Yes
Nanobeam with nanotentacles [22]	0.27	6.2	/	~5	13	Yes
Suspended nanobeam (this work)	21	43.8	>20	<4	68	Yes

voltage signal. Figure 5 shows the measured response for the device. The 10%–90% switching times are 67.0 μs and 68.8 μs for the rising edge and the falling edge, respectively, which are more than 2.5 times faster than those for the suspended-structure devices [12]. This is due to the design in which the heater is directly placed on the silicon slab to reduce the heat capacity of the device.

Table 1 compares the thermo-optic tunability of our suspended nanobeam filter with some state-of-the-art silicon thermo-optic tunable filters. It indicates that the demonstrated nanobeam filter has the highest tuning efficiency and widest tuning range.

In conclusion, we have experimentally demonstrated a single-resonance silicon PhC nanobeam filter with an ultra-high tuning efficiency. To the best of our knowledge, a record high tuning efficiency of 21 nm/mW is achieved. Only 2.214-mW heating power is needed to tune the single resonance filter over a wide spectral range of ∼43.9 nm. The results are enabled by the ultra-small mode volume of the PhC nanobeam cavity and the suspended waveguide structure. The response time is ∼68 μs by placing the microheater directly on the silicon slab. These results show a 4-fold increase in thermal tuning efficiency, and a 2.5-times faster response time relative to conventional suspended-structure silicon devices. It should be noted that as one of the main challenges for the free-standing structure, the weak mechanical stability can be improved due to the ultra-compact footprint of the PhC nanobeam cavity. The demonstrated suspended PhC nanobeam devices show the advantages of ultra-high tuning efficiency and fast response time, and can find applications in reconfigurable photonic integrated circuits including cross-bar switches and Bragg grating filters.

Funding. National Key RD Program of China (2016YFB0402501).

Acknowledgment. We thank the Center for Advanced Electronic Materials and Devices of Shanghai Jiao Tong University for the support of device fabrication.

REFERENCES

1. R. Soref, Silicon **2**, 1 (2010).
2. T. David, Z. Aaron, E. B. John, K. Tin, T. R. Graham, V. Laurent, M.-M. Delphine, C. Eric, V. Léopold, F. Jean-Marc, H. Jean-Michel, H. S. Jens, X. Dan-Xia, B. Frédéric, O. B. Peter, Z. M. Goran, and M. Nedeljkovic, J. Opt. **18**, 073003 (2016).
3. R. Soref, IEEE J. Sel. Top. Quantum Electron. **12**, 1678 (2006).
4. C. Sun, M. T. Wade, Y. Lee, J. S. Orcutt, L. Alloatti, M. S. Georgas, A. S. Waterman, J. M. Shainline, R. R. Avizienis, S. Lin, B. R. Moss, R. Kumar, F. Pavanello, A. H. Atabaki, H. M. Cook, A. J. Ou, J. C. Leu, Y.-H. Chen, K. Asanović, R. J. Ram, M. A. Popović, and V. M. Stojanović, Nature **528**, 534 (2015).
5. Y. Zhang, D. Li, C. Zeng, Z. Huang, Y. Wang, Q. Huang, Y. Wu, J. Yu, and J. Xia, Opt. Lett. **39**, 1370 (2014).
6. M. Asghari and A. V. Krishnamoorthy, Nat. Photonics **5**, 268 (2011).
7. D. A. B. Miller, Proc. IEEE **97**, 1166 (2009).
8. J. Wang, H. Shen, L. Fan, R. Wu, B. Niu, L. T. Varghese, Y. Xuan, D. E. Leaird, X. Wang, F. Gan, A. M. Weiner, and M. Qi, Nat. Commun. **6**, 5957 (2015).
9. S. Yan, X. Zhu, L. H. Frandsen, S. Xiao, N. A. Mortensen, J. Dong, and Y. Ding, Nat. Commun. **8**, 14411 (2017).
10. B. Stern, X. Zhu, C. P. Chen, L. D. Tzuang, J. Cardenas, K. Bergman, and M. Lipson, Optica **2**, 530 (2015).
11. L. Yang, T. Zhou, H. Jia, S. Yang, J. Ding, X. Fu, and L. Zhang, Optica **5**, 180 (2018).
12. P. Dong, W. Qian, H. Liang, R. Shafiiha, D. Feng, G. Li, J. E. Cunningham, A. V. Krishnamoorthy, and M. Asghari, Opt. Express **18**, 20298 (2010).
13. L. Gu, W. Jiang, X. Chen, and R. T. Chen, IEEE Photon. Technol. Lett. **19**, 342 (2007).
14. R. L. Espinola, M. C. Tsai, J. T. Yardley, and R. M. Osgood, IEEE Photon. Technol. Lett. **15**, 1366 (2003).
15. Q. Li, D. Nikolova, D. M. Calhoun, Y. Liu, R. Ding, T. Baehr-Jones, M. Hochberg, and K. Bergman, IEEE Photon. Technol. Lett. **27**, 1981 (2015).
16. F. Gan, T. Barwicz, M. A. Popovic, M. S. Dahlem, C. W. Holzwarth, P. T. Rakich, H. I. Smith, E. P. Ippen, and F. X. Kartner, *Photonics in Switching* (Optical Society of America, 2007), paper TuB3.3.
17. T. Yamane, N. Nagai, S.-i. Katayama, and M. Todoki, J. Appl. Phys. **91**, 9772 (2002).
18. M. R. Watts, W. A. Zortman, D. C. Trotter, G. N. Nielson, D. L. Luck, and R. W. Young, *Conference on Lasers and Electro-Optics and Quantum Electronics and Laser Science* (Optical Society of America, 2009), paper CPDB10.
19. Z. Lu, K. Murray, H. Jayatilleka, and L. Chrostowski, *IEEE Photonics Conference* (IEEE, 2016), paper MD3.1.
20. X. Li, H. Xu, X. Xiao, Z. Li, Y. Yu, and J. Yu, Opt. Lett. **39**, 751 (2014).
21. P. B. Deotare, M. W. McCutcheon, I. W. Frank, M. Khan, and M. LonCar, Appl. Phys. Lett. **94**, 121106 (2009).
22. J. Zhang and S. He, Opt. Express **25**, 12541 (2017).
23. K.-Y. Jeong, Y.-S. No, Y. Hwang, K. S. Kim, M.-K. Seo, H.-G. Park, and Y.-H. Lee, Nat. Commun. **4**, 2822 (2013).
24. Y. Li, J. Zhang, D. Huang, H. Sun, F. Fan, J. Feng, Z. Wang, and C. Z. Ning, Nat. Nanotechnol. **12**, 987 (2017).
25. R. Miura, S. Imamura, R. Ohta, A. Ishii, X. Liu, T. Shimada, S. Iwamoto, Y. Arakawa, and Y. K. Kato, Nat. Commun. **5**, 5580 (2014).
26. Y. Zhang, C. Zeng, H. Zhang, D. Li, G. Gao, Q. Huang, Y. Wang, J. Yu, and J. Xia, IEEE Photon. Technol. Lett. **27**, 1026 (2015).
27. W. S. Fegadolli, N. Pavarelli, P. O'Brien, S. Njoroge, V. R. Almeida, and A. Scherer, ACS Photon. **2**, 470 (2015).
28. Y. Chen, W. S. Fegadolli, W. M. Jones, A. Scherer, and M. Li, ACS Nano **8**, 522 (2014).
29. R. Soref, APL Photon. **3**, 021101 (2018).
30. H. Zhou, C. Qiu, X. Jiang, Q. Zhu, Y. He, Y. Zhang, Y. Su, and R. Soref, Photon. Res. **5**, 108 (2017).
31. Y. Zhang and Y. Shi, *IEEE International Nanoelectronics Conference* (IEEE, 2016), paper 1–2.
32. P. Sun and R. M. Reano, Opt. Express **18**, 8406 (2010).
33. L. Yu, Y. Yin, Y. Shi, D. Dai, and S. He, Optica **3**, 159 (2016).
34. J. D. Downie and A. B. Ruffin, J. Lightwave Technol. **21**, 1876 (2003).
35. P. Dong, W. Qian, H. Liang, R. Shafiiha, N.-N. Feng, D. Feng, X. Zheng, A. V. Krishnamoorthy, and M. Asghari, Opt. Express **18**, 9852 (2010).